JOURNAL OF SPACECRAFT AND ROCKETS
Vol. 58, No. 4, July–August 2021

Global Steering for Control Moment Gyroscope Clusters Using Heuristic Variable Search Techniques

Charalampos Papakonstantinou,* Vaios J. Lappas,† Hanspeter Schaub,‡ and Vassilis Kostopoulos§
University of Patras, 26504 Rio, Greece

https://doi.org/10.2514/1.A34850

This paper addresses the problem of singularity avoidance in a four-control-moment-gyroscope cluster as used for the attitude control of a satellite. A global search algorithm is developed that adjusts the null motion added upon the singularity robust inverse steering law. Its principal characteristic is that it uses global information gathered from the whole maneuver, compared to most conventional techniques that consider only some local information, near the current gimbal configuration for the optimization. The method is implemented using a ternary tree structure, and a heuristic algorithm optimizes a cost function that depends on the manipulability index, the time spent in the vicinity of singularity, the quaternion error, and the gimbal rates. Specific measures are taken to decrease the execution time of the algorithm, even for long maneuvers, without the need of a visit histogram. In addition, the tuning of only two variables can drastically change the execution time and the computational resources needed. The numerical simulation used to evaluate the algorithm indicates that the elliptic singularity can sufficiently be avoided and the algorithm drives the system fast away from the singularity with an overall performance improvement.

Nomenclature

$\boldsymbol{A}(\boldsymbol{\delta})$	=	Jacobian matrix
$\boldsymbol{A}^{\#}(\boldsymbol{\delta})$	=	inverse of the Jacobian matrix
D	=	tree depth
dt	=	time-step
g_1, g_2, g_3, g_4	=	cost function coefficients
$\boldsymbol{H}$	=	spacecraft angular momentum vector
$\dot{\boldsymbol{H}}$	=	time derivative of spacecraft angular momentum vector
$\boldsymbol{h}$	=	control-moment-gyroscope angular momentum vector
$\boldsymbol{h}_c$	=	commanded momentum vector
h_m	=	mean maximum angular momentum
h_0	=	magnitude of momentum of each flywheel
$\dot{\boldsymbol{h}}$	=	time derivative of control-moment-gyroscope angular momentum vector
I_{exec}	=	execution index
K_p, K_ω	=	controller gains
$k_{\max}$	=	maximum null-motion value
$\boldsymbol{L}$	=	null-motion set
$\boldsymbol{q}$	=	quaternion vector
$\boldsymbol{q}_{\text{des}}$	=	desired quaternion vector
$\boldsymbol{q}_{\text{err}}$	=	quaternion error vector
$\boldsymbol{q}_i$	=	quaternion vector in ith iteration
$\boldsymbol{q}_{\text{ini}}$	=	initial quaternion vector
$\dot{\boldsymbol{q}}$	=	time derivative of quaternion vector
$\boldsymbol{q}^*_{\text{des}}$	=	conjugate of quaternion vector
$\|\boldsymbol{q}^v_{\text{err}}\|_{\max}$	=	maximum norm of the quaternion error vector across the trajectory
$\text{skip}_{\text{rate}}$	=	number of children skipped by the algorithm
skip_{th}	=	threshold of children skipped by the algorithm
$\boldsymbol{T}_c$	=	control torque vector
$\boldsymbol{T}_{\text{cmg}}$	=	torque vector created by control moment gyroscope
$\boldsymbol{T}_{\text{ex}}$	=	external torques vector
$T_{\max\{\dot\delta_1,\dot\delta_2,\dot\delta_3,\dot\delta_4\}>\dot\delta_{\text{th}}}$	=	term proportional to the time the gimbal rates exceed a specific threshold
$T_{w<w_{\text{th}}}$	=	term proportional to the time the manipulability index is below a specific threshold
w	=	manipulability index
w_{mean}	=	mean value of manipulability along the trajectory
w_{th}	=	manipulability index threshold
β	=	skew angle
$\boldsymbol{\delta}$	=	gimbal angles vector
$\dot{\boldsymbol{\delta}}$	=	time derivative of gimbal angles' vector
$\dot{\boldsymbol{\delta}}_{\text{Null}}$	=	time derivative of gimbal angles' vector that belongs in the null space
$\dot{\boldsymbol{\delta}}_{\text{sat}}$	=	saturated gimbal rates vector
$\dot\delta_{\text{th}}$	=	gimbal rates saturation threshold
λ_0	=	steering law gain
$\boldsymbol{\omega}$	=	spacecraft angular velocity vector

I. Introduction

CONTROL moment gyroscopes (CMGs) are widely used in spacecraft control for maneuvering, and they have been successfully employed for a wide range of space missions [1–3]. A single-gimbal control moment gyroscope is a device consisting of a spinning wheel that rotates at a constant rate attached on a gimbal motor. Taking advantage of the torque amplification effect, they are ideal for nanosized missions through a miniaturization process [4,5]. The main concern of a CMG cluster is that it may be unable to generate the required torque in certain configurations, and such states are referred as singularities. There are two types of singularities regarding the ability to escape from the singular state by null motion [6]. If the singularity cannot be escaped by null motion, it is classified as elliptic. Otherwise, the singularity is passable or hyperbolic. Singularities presented in such systems are commonly avoided by steering laws that make use of some local information in the vicinity of the current gimbal configuration [7,8]. This information is usually related to the manipulability index as a performance measure [9], but a variety of indices are also presented in Ref. [10]. Commonly well-known steering laws often use

Received 10 May 2020; revision received 5 November 2020; accepted for publication 5 November 2020; published online 20 January 2021.

*Ph.D. Student, Department of Mechanical Engineering and Aeronautics; c_papakonstantinou@upnet.gr.

†Research Professor, Department of Mechanical Engineering and Aeronautics; vlappas@upatras.gr. Senior Member AIAA.

‡Professor, Aerospace Engineering Sciences Department, Colorado Center for Astrodynamics Research, University of Colorado, Boulder, CO 80303-0429; hanspeter.schaub@colorado.edu.

§Professor, Department of Mechanical Engineering and Aeronautics; Director of Applied Mechanics and Vibrations Laboratory; kostopoulos@upatras.gr.

the redundancy of the gimbals in a four-CMG cluster. While a CMG can easily encounter singularities, a variable-speed CMG (VSCMG) introduces four extra degrees of freedom, which can be used to avoid these singularities, although it is similarly engineered [11]. VSCMGs have also been used for power management [12–15], whereas a novel approach of combining a VSCMG with a double-gimbal CMG is presented in Refs. [16,17]. Allowing a standard double-gimbal gyroscope to change the flywheel speed provides additional torquing capabilities, which are significant in case of failures.

In general, the methods of path planning a maneuver so far are focusing on choosing the initial gimbal configuration that optimizes the performance of the system during the trajectory [18,19]. That means that the gimbals are guided to a certain configuration before executing the maneuver, and a similar work has been presented in Ref. [20]. A different path planning technique that combines the pseudospectral and the direct shooting methods upon gimbal saturation and singularity constraints is presented in Ref. [21]. In Ref. [22] is also described an energy-consumption-based path planning technique for double-gimbal CMGs. A global singularity avoidance steering law is explored in Ref. [23], where the time integral of the quadratic sum of the gimbal rates is minimized; and a trajectory planning approach is used in Ref. [24] to reduce the possibility of CMG saturation while following a reference path. In this paper, though, a heuristic method is presented that combines the information of the manipulability index, the off-axis error, and gimbal rates through the whole trajectory and optimizes a cost function subject to a null motion added upon the singularity robust inverse (SRI) steering law. In contrast to previous studies where the null motion guides the gimbal angles to an optimized configuration before executing the desired maneuver, in this paper, the reconfiguration of the gimbal angles takes place during the maneuver. The work discussed in Refs. [25,26], where a global approach is analyzed and a mission planning technique is presented, is unable to follow the needs of a near-real-time application. Moreover, it is limited to exploring the optimal path in the configuration space between two points only in the momentum space without taking into consideration the dynamic characteristics of the system. The algorithm is based on an A* search with enhanced features, as the two-dimensional histogram and the "cost cutoff" variable.

The novel algorithm proposed in this paper can be executed either online or offline, enabling the inspection of the motion as long as the model of the satellite is available and it can be applied for arbitrary maneuver and initial configuration. It can also be applied either for the kinematic or the complex (dynamics and kinematics) model. It demonstrates enhanced features compared to published work, such as lower execution time and less memory allocation. It consists of an application, of which the execution time can be directly controlled by modifying only two variables. In particular, a ternary tree structure is used where every child represents a different null motion and a heuristic algorithm is used to select the best children. A ternary tree is a tree data structure similar to a binary tree, but every parent has three children expanded in each level. The heuristic algorithm used is implemented in a tree structure because the null motion is expanded for every time step, starting from the root and exploring every branch as far as possible (depending on the cost function) before backtracking and searching for other solutions. The purpose of including the null motion in the system is to assist the singularity robust inverse steering law to pass by the singularity. The goal in this paper is to find a path that improves the value of the cost function compared to the case where only the SRI is applied. Therefore, the algorithm does not necessarily provide a singularity-free path. However, following a strategy similar to the one referred in Ref. [18], which reorients the CMGs to a high-performance configuration, the optimization can also be applied before executing the commanded maneuver. In contrast to the preferred angles approach, this method has the advantage of not requiring the knowledge of the torque and the angular momentum profiles to be known a priori; and the backintegration process is not present, thus saving time and allowing easier onboard implementation on a satellite. However, the requirement of more than three CMGs in the cluster still remains in order to exploit the redundancy of the system.

The paper is structured as follows. In Sec. II, the rigid spacecraft equations of motion are described; and Sec. III presents the global search algorithm. Any simulation assumption and specification are given in the Simulation Setup section (Sec. IV), and the results are presented and discussed in the two last sections. A comparison is held between the two models and the work presented in Ref. [25].

II. Mathematical Modeling

The equation of motion of a rigid spacecraft is described by

$$\dot{\boldsymbol{H}} + \boldsymbol{\omega} \times \boldsymbol{H} = \boldsymbol{T}_{\text{ex}} + \boldsymbol{T}_{\text{cmg}} \tag{1}$$

where $\boldsymbol{T}_{\text{ex}} \epsilon \Re^{3\times1}$ is the vector that contains the external torques applied to the spacecraft, $\boldsymbol{H} \epsilon \Re^{3\times1}$ represents the total angular momentum of the spacecraft, and $\boldsymbol{\omega} \epsilon \Re^{3\times1}$ represents the angular velocity of the spacecraft with respect to the body frame. In this paper, the notation $\dot{(\cdot)}$ indicates the time derivative of $(\cdot)$. $\boldsymbol{T}_{\text{cmg}}$ is the total torque applied to the spacecraft, created by the CMGs, which is equal to the momentum rate of the cluster. A control torque $\boldsymbol{T}_c \epsilon \Re^{3\times1}$ can be selected as [27]

$$\dot{\boldsymbol{h}} + \boldsymbol{\omega} \times \boldsymbol{h} = -\boldsymbol{T}_c \tag{2}$$

where $\boldsymbol{h} \epsilon \Re^{3\times1}$:

$$\boldsymbol{h} = h_0 \begin{bmatrix} -c\beta s\delta_1 - c\delta_2 + c\beta s\delta_3 + c\delta_4 \\ c\delta_1 - c\beta s\delta_2 - c\delta_3 + c\beta s\delta_4 \\ s\beta s\delta_1 + s\beta s\delta_2 + s\beta s\delta_3 + s\beta s\delta_4 \end{bmatrix} \tag{3}$$

is the angular momentum of the CMG; and s and c are the abbreviations for sin and cos, respectively. The parameter β denotes the skew angle of the four-CMG cluster in the pyramid configuration, and it is chosen in such a way that the momentum envelope is nearly tree-axis symmetric and spherical [28]. Also, h_0 is the magnitude of the momentum of each flywheel. The mean maximum angular momentum h_m as described in Ref. [29] is given by

$$h_m \approx 2h_0(1 + \cos\beta) \tag{4}$$

In general, the momentum derived from the CMG cluster is a function of the gimbal angles $\boldsymbol{\delta} = [\delta_1, \delta_2, \delta_3, \delta_4]^T \epsilon \Re^{4\times1}$ for a spacecraft employed with four CMGs. Assuming that the control torque is known, the relation between the total CMG momentum rate and the gimbal angles rates can be derived by the equation

$$\dot{\boldsymbol{h}} = \boldsymbol{A}(\boldsymbol{\delta})\dot{\boldsymbol{\delta}} \tag{5}$$

The matrix $\boldsymbol{A}(\boldsymbol{\delta}) \epsilon \Re^{3\times4}$ is the Jacobian matrix of the system and, except for the gimbal angles, the Jacobian matrix depends on geometric characteristics of the CMGs like the skew angle. For the four-CMG cluster, the Jacobian matrix is given by

$$\boldsymbol{A}(\boldsymbol{\delta}) = \begin{bmatrix} -c\beta c\delta_1 & s\delta_2 & c\beta c\delta_3 & -s\delta_4 \\ -s\delta_1 & -c\beta c\delta_2 & s\delta_3 & c\beta c\delta_4 \\ s\beta c\delta_1 & s\beta c\delta_2 & s\beta c\delta_3 & s\beta c\delta_4 \end{bmatrix} \tag{6}$$

The gimbal angle rate vector $\dot{\boldsymbol{\delta}} \epsilon \Re^{4\times1}$ can be calculated by

$$\dot{\boldsymbol{\delta}} = \boldsymbol{A}^{\#}(\boldsymbol{\delta})\dot{\boldsymbol{h}} \tag{7}$$

Since the Jacobian matrix is not rectangular and the inverse of the matrix cannot be calculated, several definitions have been proposed for the inverse of the Jacobian matrix $\boldsymbol{A}^{\#}(\boldsymbol{\delta})$ [30,31].

The satellite's kinematic equations of motion expressed in quaternion form are given by

$$\dot{\boldsymbol{q}} = \frac{1}{2}\boldsymbol{q}\odot\boldsymbol{\omega}_q \tag{8}$$

where $\odot$ denotes the quaternion multiplication, $\boldsymbol{q} = [q_0, q_1, q_3, q_4]^T \epsilon \Re^{4\times1}$ represents the attitude quaternion, and $\boldsymbol{\omega}_q$ is the quaternion that consists of the angular velocity $\boldsymbol{\omega}$ of the satellite as $\boldsymbol{\omega}_q = [0, \boldsymbol{\omega}^T]^T \epsilon \Re^{4\times1}$. For two quaternions $\boldsymbol{r} = [r_0, r_1, r_2, r_3]^T \epsilon \Re^{4\times1}$ and $\boldsymbol{p} = [p_0, p_1, p_2, p_3]^T \epsilon \Re^{4\times1}$, the quaternion multiplication is given by

$$\boldsymbol{r}\odot\boldsymbol{p} = \begin{bmatrix} p_0r_0 - p_1r_1 - p_2r_2 - p_3r_3 \\ p_0r_1 + p_1r_0 - p_2r_3 + p_3r_2 \\ p_0r_2 + p_2r_0 + p_1r_3 - p_3r_1 \\ p_0r_3 - p_1r_2 + p_2r_1 + p_3r_0 \end{bmatrix} \tag{9}$$

For the implementation of the attitude control, the control torque $\boldsymbol{T}_c$ applied on the satellite's body is a function of the vector part of the error quaternion $\boldsymbol{q}_{\text{err}}$ and $\boldsymbol{\omega}$ as described by the following equation:

$$\boldsymbol{T}_c = -(K_p\boldsymbol{q}_{\text{err}}^v + K_\omega\boldsymbol{\omega}) \tag{10}$$

The quaternion error between the current attitude quaternion and a desired quaternion $\boldsymbol{q}_{\text{des}}$ is

$$\boldsymbol{q}_{\text{err}} = \begin{bmatrix} q_{\text{err}}^s \\ \boldsymbol{q}_{\text{err}}^v \end{bmatrix} = \boldsymbol{q}_{\text{des}}^*\odot\boldsymbol{q} \tag{11}$$

where q_{err}^s and $\boldsymbol{q}_{\text{err}}^v = [q_{\text{err}}^{\text{roll}}, q_{\text{err}}^{\text{pitch}}, q_{\text{err}}^{\text{yaw}}]^T$ are the scalar and the vector parts, respectively; and $\boldsymbol{q}_{\text{des}}^*$ expresses the conjugate quaternion of $\boldsymbol{q}_{\text{des}}$. The normalization of the quaternions is required before evaluating the $\boldsymbol{q}_{\text{err}}$. The "3-2-1" sequence is used to convert the quaternion error to the corresponding Euler angles error. To guarantee the attitude stability of the spacecraft, consider the following the candidate Lyapunov function [32–34]:

$$V = \frac{1}{2}\boldsymbol{\omega}^{\text{T}}\boldsymbol{J}\boldsymbol{\omega} + K_p{\boldsymbol{q}_{\text{err}}^v}^{\text{T}}\boldsymbol{q}_{\text{err}}^v + K_p(1-q_0)^2 \tag{12}$$

The first time derivative of V is given by

$$\dot{V} = \boldsymbol{\omega}^T\boldsymbol{J}\dot{\boldsymbol{\omega}} + K_p{\dot{\boldsymbol{q}}_{\text{err}}^v}^T\boldsymbol{q}_{\text{err}}^v + K_p{\boldsymbol{q}_{\text{err}}^v}^T\dot{\boldsymbol{q}}_{\text{err}}^v - 2\eta(1-q_0)\dot{q}_0 \tag{13}$$

Because $\boldsymbol{q}_{\text{err}}^{v\,T}\dot{\boldsymbol{q}}_{\text{err}}^v$ is a scalar, the following can be shown:

$${\boldsymbol{q}_{\text{err}}^v}^T\dot{\boldsymbol{q}}_{\text{err}}^v = (\dot{\boldsymbol{q}}_{\text{err}}^{v\,T}\boldsymbol{q}_{\text{err}}^v)^T = \dot{\boldsymbol{q}}_{\text{err}}^{v\,T}\boldsymbol{q}_{\text{err}}^v \tag{14}$$

and Eq. (13) becomes

$$\dot{V} = \boldsymbol{\omega}^T\boldsymbol{J}\dot{\boldsymbol{\omega}} + 2K_p{\dot{\boldsymbol{q}}_{\text{err}}^v}^T\boldsymbol{q}_{\text{err}}^v - 2\eta(1-q_0)\dot{q}_0 \tag{15}$$

Because ${\boldsymbol{q}_{\text{err}}^v}^T S(\boldsymbol{\omega})\boldsymbol{q}_{\text{err}}^v = 0$, where $S(\boldsymbol{\omega})$ is the skew matrix of $\boldsymbol{\omega}$, and substituting Eq. (1) into Eq. (15),

$$\dot{V} = \boldsymbol{\omega}^T(\boldsymbol{J}\dot{\boldsymbol{\omega}} + K_p\boldsymbol{q}_{\text{err}}^v) \tag{16}$$

Equation (16) can be simplified as

$$\dot{V} = \boldsymbol{\omega}^T(-\boldsymbol{\omega}\times\boldsymbol{J}\boldsymbol{\omega} - K_w\boldsymbol{\omega}) \tag{17}$$

Note that $\boldsymbol{\omega}^T(\boldsymbol{\omega}\times\boldsymbol{J}\boldsymbol{\omega}) = 0$. Finally,

$$\dot{V} = -\boldsymbol{\omega}^T K_w\boldsymbol{\omega} \tag{18}$$

and the global stability is guaranteed for $K_w > 0$ [35].

III. Global Search

Most singularity avoidance methods make use of some local information, optimizing a factor in the current gimbal configuration. In this section, a method that takes into consideration a cost function through the whole maneuver is proposed. The SRI steering law as given in Ref. [36] is

$$\boldsymbol{A}^{\#} = \boldsymbol{A}^T(\boldsymbol{A}\boldsymbol{A}^T + \lambda\boldsymbol{I}_3)^{-1} \tag{19}$$

where $\boldsymbol{I}_3$ is the three-by-three identity matrix. The gain λ is calculated by

$$\lambda = \lambda_0 e^{-\mu w} \tag{20}$$

and depends on a performance index w, which is a measure of the linear independence of the columns of matrix $\boldsymbol{A}$, usually referred to as the manipulability index:

$$w = \sqrt{\det(\boldsymbol{A}\boldsymbol{A}^T)} = |\sigma_1\sigma_2\sigma_3| \tag{21}$$

Also, $|\sigma_1\sigma_2\sigma_3|$ denotes the absolute value of the product of the singular values of $\boldsymbol{A}$. When $\boldsymbol{A}$ is to become singular, at least one of the σ_1, σ_2, and σ_3 tends to zero; and this property allows us to use it as a measure of closeness to singularity. The null-motion term is added in Eq. (7) and is composed of the term k_i and the null gimbal rates $\dot{\boldsymbol{\delta}}_{\text{Null}} \epsilon \Re^{4\times1}$ as

$$\dot{\boldsymbol{\delta}} = \boldsymbol{A}^{\#}(\boldsymbol{\delta})\dot{\boldsymbol{h}} + 4k_i\dot{\boldsymbol{\delta}}_{\text{Null}} \tag{22}$$

where

$$\dot{\boldsymbol{\delta}}_{\text{Null}} = [|c_2\ c_3\ c_4|,\ -|c_2\ c_3\ c_4|,\ |c_2\ c_3\ c_4|,\ -|c_2\ c_3\ c_4|]^T \tag{23}$$

and $\boldsymbol{c}_N \epsilon \Re^{3\times1}$ represents the output torque of the Nth CMG of the cluster, i.e., the Nth column of $\boldsymbol{A}$. Let the value of k_i change in each time step resulting in a different null motion. The proposed method optimizes the set

$$\boldsymbol{L} = [k_1, k_2, \ldots, k_{st}] \tag{24}$$

where k_i denotes the null-motion value at time i, and st is the total simulation time. The cost function that has to be maximized is the following:

$$\text{CF} = \frac{g_1 w_{\text{mean}}}{g_2 T_{w<w_{\text{th}}} + g_3\|\boldsymbol{q}_{\text{err}}^v\|_{\max} + g_4 T_{\max\{\dot{\delta}_1,\dot{\delta}_2,\dot{\delta}_3,\dot{\delta}_4\}>\dot{\delta}_{\text{th}}}} \tag{25}$$

where w_{mean} is the mean value of the manipulability index over the trajectory; $T_{w<w_{\text{th}}}$ is proportional to the time; the manipulability index is below a specific threshold w_{th} for a trajectory with n discrete steps; and g_1, g_2, g_3, and g_4 have a constant value. The term $\|\boldsymbol{q}_{\text{err}}^v\|_{\max}$ expresses the maximum norm of the quaternion error vector across the trajectory. This error includes the controller error for the commanded maneuver and the off-axis error, which is added upon the controller error as introduced by the SRI. The controller error cannot be optimized, but it is used to prevent the denominator from being zero when the remaining two terms are zero. In practice, the off-axis error is the subject of optimization for the third term of the cost function (CF). The last term prevents the search algorithm from selecting nodes that result in gimbal rates that are above a preset threshold $\dot{\delta}_{\text{th}}$ and is proportional to the time $T_{\max\{\dot{\delta}_1,\dot{\delta}_2,\dot{\delta}_3,\dot{\delta}_4\}>\dot{\delta}_{\text{th}}}$ the gimbal rates exceed this limit. The first, the second, and the last terms in the CF are related to the gimbal angles and, as a consequence, to the gimbal rates. The third term is indirectly related to the gimbal rates because the rates determine the attitude of the cluster. Hence, the value of k_i is related to the CF through Eq. (22), which determines the gimbal rates. The search algorithm consists of a heuristic approach where each node represents

a different value of k_i in the tree level i. A number of child nodes expanded from a parent node span the range of possible null motions. The method expands three children per parent: one each for negative, zero, and positive null motions. Thus, there are three different values of k_i: $-k_{\max}, 0$, and $+k_{\max}$, where $k_{\max}$ is a constant value that represents the maximum null motion that can be added to the system in each time step. The first time the algorithm is executed, the value of the cost function is set as the best value and the search is similar to that of a gradient method. For the next searches, each time the algorithm reaches the terminal child, the value of the cost function is compared to the best value so far and replaced if needed. In the end of the algorithm, the length of the $\boldsymbol{L}$ set is equal to st, which is the same as the tree depth D.

For a tree depth D, the terminal children may be 3^D (Fig. 1).

To overcome the problem of the high computational cost needed to execute this amount of calculations, a variable search density approach is developed. This approach is implemented by varying the number of children the algorithm skips to search $\text{skip}_{\text{rate}}$ every time the value is worse than the best value. To prevent the search from skipping uncontrollably, a large amount of the children (a skip threshold skip_{th}) is used. In Fig. 2, a simple example for $\text{skip}_{\text{th}} = 2$ is presented. Trying to maximize the cost function value, it is noticed that this technique manages to skip paths that lead to lower cost function values, saving computational resources and time. However, the solution is suboptimal because the third child, which results in the best cost function value, has been skipped. The underlined numbers denote when the algorithm discovers a new best value and the $\text{skip}_{\text{rate}}$ is reset.

As a result, the branches of the tree become denser near high cost function values and sparser near lower values. Varying the "skip" parameter of the algorithm, a tradeoff takes place between the computational time and how close to the optimal solution the result is. In Fig. 3, a visualization of the tree presents the dense and sparse areas where the lines are getting thicker and thinner, respectively.

IV. Simulation Setup

A specific task is selected to evaluate the efficiency of the method near an internal elliptic singularity. The four-CMG cluster is in an elliptic singularity when the gimbal angles are equal to $\boldsymbol{\delta} = [-90, 0, 90, 0]^T$ deg [37]. This can be easily proven as follows:

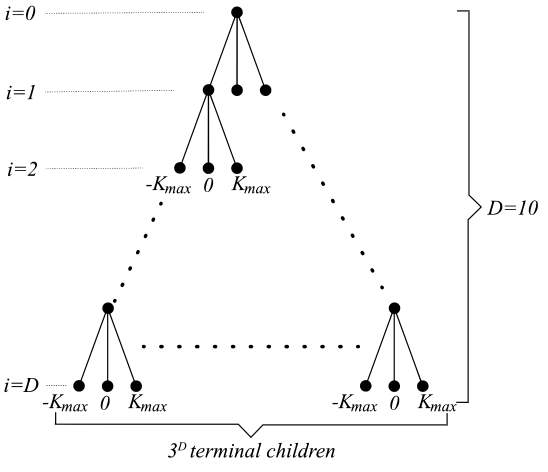

Fig. 1 Tree structure.

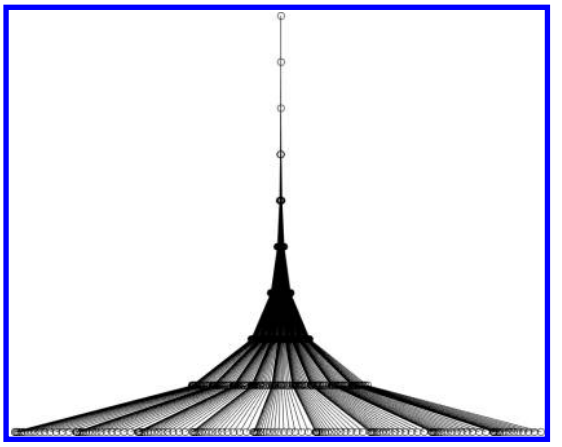

Fig. 3 Tree visualization.

$$\boldsymbol{A}(-90,0,90,0) = \begin{bmatrix} 0 & 0 & 0 & 0 \\ 1 & -0.5774 & 1 & 0.5774 \\ 0 & 0.8164 & 0 & 0.8164 \end{bmatrix}$$

$$\boldsymbol{N} = \text{null}(\boldsymbol{A}) = \begin{bmatrix} -0.7071 & -0.3536 \\ 0.0000 & -0.6124 \\ 0.7071 & -0.3536 \\ -0.0000 & 0.6124 \end{bmatrix}$$

$$\boldsymbol{u} = \text{null}(\boldsymbol{A}^T) = \begin{bmatrix} 1, 0, 0 \end{bmatrix}^T$$

$$\boldsymbol{E} = \text{diag}(\boldsymbol{u}^T \boldsymbol{h}_N) = \text{diag}(0.5774, -1, 0.5774, 1)$$

$$\boldsymbol{M} = \boldsymbol{N}^T \boldsymbol{E} \boldsymbol{N} = \begin{bmatrix} 0.5774 & 0 \\ 0 & 0.1444 \end{bmatrix} \tag{26}$$

The determinant of matrix $\boldsymbol{M}$ is obviously positive, meaning that $\boldsymbol{M}$ is definite and the configuration corresponds to an elliptic singularity. The exact simulation parameters used are shown in Table 1. The task is selected to be a maneuver in roll axis by -90 deg because the system encounters this elliptic singularity as long as the proper initial angles are used. Two different cases are examined. In the first, the kinematics and the dynamics equations of the system are implemented (complex model). The initial gimbal configuration is $\boldsymbol{\delta}_{\text{ini}} = [-70, 0, 75, 0]$ deg, and the initial attitude quaternion is $\boldsymbol{q}_{\text{ini}} = [1, 0, 0, 0]^T$. The system is commanded to follow the desired orientation given by the quaternion $\boldsymbol{q}_{\text{des}} = [0.70711, -0.70711, 0, 0]^T$. A visualization of the pyramid cluster in the initial configuration can be seen in Fig. 4.

Even if the initial configuration and the selected maneuver are not usual or practical for real-life satellite applications, dealing with the worst-case scenario is a simulation strategy that enables us to prove that the proposed global steering method is effective in challenging conditions; and it showcases advantages and limitations as done in the literature [7,18,27]. In this paper, a single-axis maneuver is explored but the method is adaptable to every case as long as the initial configuration and the commanded maneuver are given. In the second case, only the kinematic model of the system is used; there is no quaternion based feedback controller, and the input of the system is the difference between the current momentum and the commanded momentum over the time dt. As no quaternions are used in this

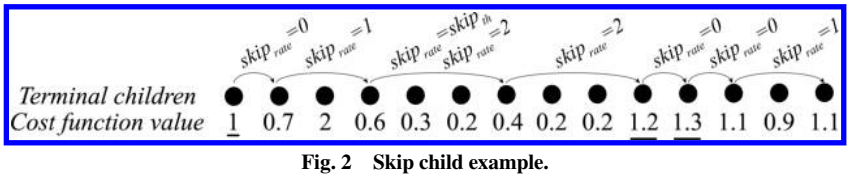

Fig. 2 Skip child example.

Table 1 Simulation parameters

Parameter	Complex model	Kinematics-only model
Maneuver, deg	0 to −90	0 to −90
Moment of inertia $\boldsymbol{J}$, kg/m^2	diag([1, 1, 1])	diag([1, 1, 1])
Momentum h_0, N · m · s	1	1
Time step dt, s	0.1	0.1
Simulation time, s	7	7
K_p, K_ω	20, 15	— —
$\boldsymbol{h}_c$	— —	$[1.5 \quad 0 \quad 0]^T$ N · m · s
Skew angle β, deg	54.73	54.73
$\dot{\delta}_{\text{th}}$, deg/s	50	50
$\boldsymbol{\delta}_{ini}$, deg	$[-70, 0, 75, 0]^T$	$[0, 0, 0, 0]^T$
$k_{\max}$	0.7	0.7
λ_0	1	1
μ	0.2	0.2
w_{th}	0.5	0.5
g_1, g_2, g_3, g_4	300, 5, 4, 6	300, 50, 4, 6
D	10	10
$\text{skip}_{\text{rate}}$	Variable in [0, 250]	Variable in [0, 250]
skip_{th}	250	250

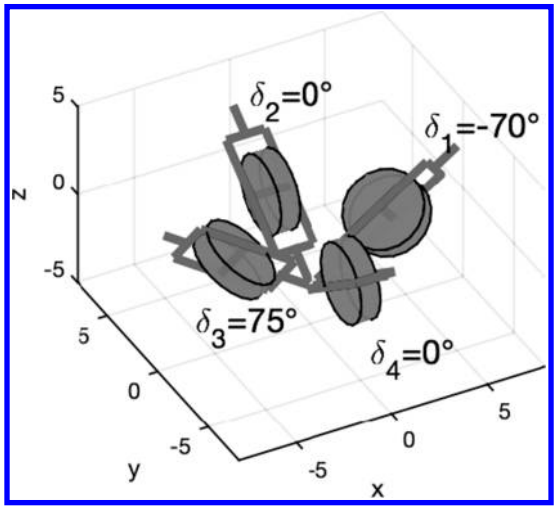

Fig. 4 Cluster visualization.

case, the third term in Eq. (25) is replaced by the maximum norm torque error through the trajectory. The initial gimbal configuration is $\boldsymbol{\delta}_{\text{ini}} = [0, 0, 0, 0]$ deg. For encountering an elliptic singularity for the specific initial configuration, the commanded momentum $\boldsymbol{h}_c$ should be more than 1.15 N · m · s in the x axis [38], and so $\boldsymbol{h}_c = [1.5 \quad 0 \quad 0]^T$ N · m · s is selected. For the complex and the kinematics-only models, the total simulation time is 7 s. To better match the limitations of a real CMG cluster, the CMG gimbal angle rates reach the saturation when they exceed the specific threshold $\dot{\delta}_{\text{th}}$ through the following formula:

$$\dot{\boldsymbol{\delta}}_{\text{sat}} = \dot{\boldsymbol{\delta}} \frac{\dot{\delta}_{\text{th}}}{\max(|\dot{\delta}_1|, |\dot{\delta}_2|, |\dot{\delta}_3|, |\dot{\delta}_4|)} \tag{27}$$

It is preferred to saturate the gimbal angle rates using Eq. (27) over applying a boundary value to every gimbal angle rate that exceeds the required threshold because the characteristics of the motion are conserved. To achieve null motion in each simulation time step dt for a 15 s simulation, a tree depth of $D = 150$ is required. Such a depth is not practical for real applications, and a much lower value is used ($D = 10$). That means that the number of elements in the $\boldsymbol{L}$ set is different than st. To obtain a k_i value for every time step, the $\boldsymbol{L}$ set is interpolated through the simulation time. In Fig. 5, two different approaches for interpolation are presented for a total simulation time equal to 0.15 s and $D = 3$. Also, $k_{\max}$ is constant and is ignored in the figure for simplicity. The first (Fig. 5a) approach is similar to a zero-order-hold (ZOH) filter, whereas the second (Fig. 5b) is a linear interpolation. In this paper, the linear interpolation is used.

V. Simulation Results

In oder to evaluate the method proposed in this paper, a comparison between a single-axis CMG-based maneuver that uses a conventional SRI steering logic and is compared to the method proposed in this paper.

A. Complex Model

In the first simulation, the search algorithm is not applied and the system makes use only of the SRI steering law as the singularity avoidance mechanism. The results are presented in Fig. 6. At $t = 0$ s, the system is commanded to follow the desired attitude quaternion. The $\boldsymbol{L}$ set in this case is $\boldsymbol{L} = k_{\max}[0, 0, 0, 0, 0, 0, 0, 0, 0, 0]$, and the value of the cost function is equal to 0.129. As seen in Figs. 6a and 6d the attitude angle about the roll axis reaches the value of −86.25 deg at $t = 7$ s. The SRI steering law is responsible for the deviation in the attitude angle and the attitude error about the pitch and yaw axis from $t = 0.5$ s to $t = 6$ s as the system approaches the singularity. The maximum absolute deviations in the pitch and yaw axes are 18 and 5 deg, respectively. The maximum angular velocity as seen in Fig. 6b is about the roll axis, but high velocities are presented to the rest axes as well. In the beginning, the angular momentum in the x axis is stuck to 1.15 N · m · s; whereas the rest of the components are nearly zero (Fig. 6c), which is an indication that the system is in a singular state in this period of time, as referred to in the previous section. When the momentum in the z axis starts to rise, the satellite is starting to deviate from the desired trajectory and passes by the low-performance configuration. The attitude error goes to zero at the end of the simulation, when the system passes the singularity, reaching the commanded attitude. Figure 6e shows that the gimbal angles in the beginning of the simulation are nearly $[-90, 0, 90, 0]^T$ until $t = 1.2$ s, indicating that the system is close to an elliptic singular state. As a result, no torque is generated by the cluster, as shown in Fig. 6g for this time period. At the same time, the manipulability index (Fig. 6h) approaches and remains zero until the steering law starts to generate the off-axis error. Then, the system escapes the singularity and the value of the index in the steady state becomes equal to 0.609. In addition, the rate of the second gimbal remains saturated from $t = 2s$ to $t = 3.3$ s, scaling the rates of the rest gimbals according to Eq. (27). Overall, the SRI steering law is capable of avoiding the low-performance configurations, generating attitude error; but, the specific tuning is driving the system fast into the singularity. It is expected that when the global optimization algorithm is applied, the null space motion reconfigures the gimbal angles to values that is easier for the cluster to avoid the elliptic singularity.

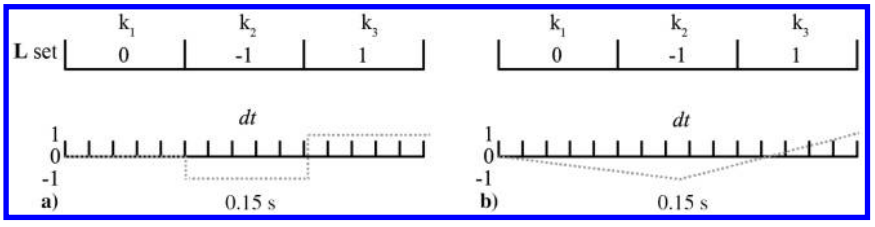

Fig. 5 Interpolation approaches: a) ZOH and b) linear.

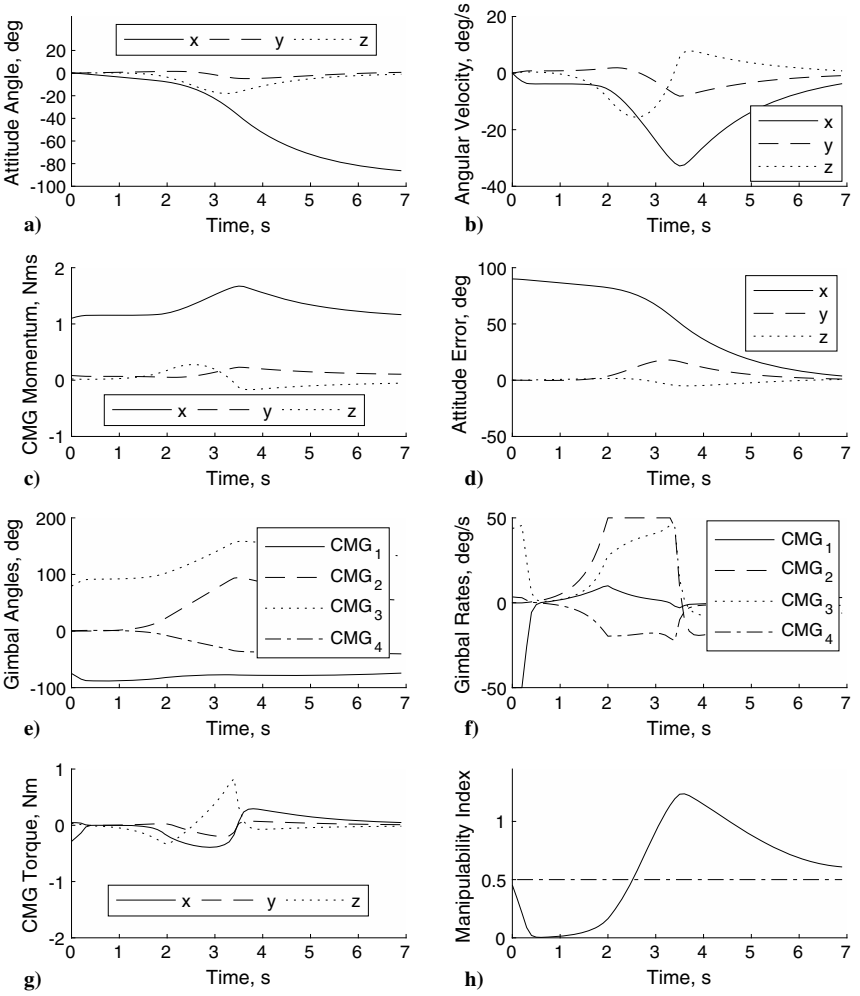

Fig. 6 Results derived without using search algorithm for dynamic and kinematic models: a) attitude angle, b) angular velocity, c) CMG momentum, d) attitude error, e) gimbal angles, f) gimbal rates, g) CMG torque, and h) manipulability index.

The second simulation uses the global optimization algorithm as described in Eqs. (19–25), and the results are shown in Fig. 7. The $\boldsymbol{L}$ set in this case is $\boldsymbol{L} = k_{\max}[1, 1, 0, -1, 0, 0, 0, 0, 0, 0]$, indicating the importance of the null space motion near the beginning of the motion slightly before the singularity occurs. The manipulability index is taken into consideration near the beginning of the simulation in order to drive the system to a better performance configuration before the SRI creates the off-axis error. This strategy assists the system in obtaining a better mean manipulability value while SRI is creating the error upon the trajectory. In contrast, in the steady state, no gimbal reconfiguration takes places. In Table 2, the percentage change is presented for each CF term compared to the first simulation. There is a 99.3% increase in the cost function value compared to the first simulation, and significant improvements of 85.1 and 50% are presented in the mean value of the manipulability index and the $T_{w<w_{\text{th}}}$ term, which is proportional to the time this index remains below the preset threshold. However, there is a slight difference in the attitude angle and error, the angular velocity, and the CMG momentum profile, as shown in Figs. 7a–7d. The difference in the attitude angle and error profile is presented about the pitch and yaw axes that start to deviate from zero earlier. The same applies for the angular velocity of the satellite and the momentum of the CMG cluster. As shown in Fig. 7e, the second and the fourth gimbal angles start to deviate from zero at $t = 0$ s, getting far from $[-90, 0, 90, 0]^T$, which is the key to preventing the system from spending a long time in the vicinity of the singularity. The combination of the null motion that starts in the beginning of the simulation and the simultaneous attitude error generated by the SRI result in a higher cost function value. There is also a minor improvement in the settling time because the attitude angle about the roll axis is -87.7 deg at $t = 7$ s. The momentum of the cluster passes through $[1.5 \quad 0 \quad 0]^T$ N · m · s without being locked in this state, but there is a noticeable increase in the time the gimbal motors remain saturated (Fig. 7f).

This is the natural drawback to exploiting the null motion because the motors are used to rotate the gimbals to proper positions for a longer period of time. Even though a lower $k_{\max}$ value reduces the time the gimbal rates spend in saturation, the cost function value becomes lower and the motions/results begin to look similar to those of the first simulation.

A similar profile as in the first simulation is obtained for the CMG torque about the roll axis (Fig. 7g), but no torque gaps are presented in between the motion as happens in the first simulation. The torque about the roll spans in the negative of the axis until $t = 2.2$ s when the direction changes in order to decelerate the satellite. A significant difference is observed in the manipulability index (Fig. 7h). It starts from the same value as in the first simulation, but there is a noticeable decrease of 50% in the time it remains below the preset threshold and an 85.1% increase in its mean value. The horizontal dashed line indicates the value of the threshold w_{th}. Inevitably, the global optimization algorithm increases the power demands of the system because the gimbal motors are exploited not only for executing the desired maneuver but also for optimizing the given criteria.

In general, the coefficients g_1, g_2, g_3, and g_4 have to be selected according to the application. For example, a 20 times larger value of g_4 for the same g_1, g_2, and g_3 values results in different gimbal rate profiles, where the rates do not remain saturated for such a long period of time. However, the system remains near the singularity for a longer period of time. In this paper, the coefficients are selected mainly to

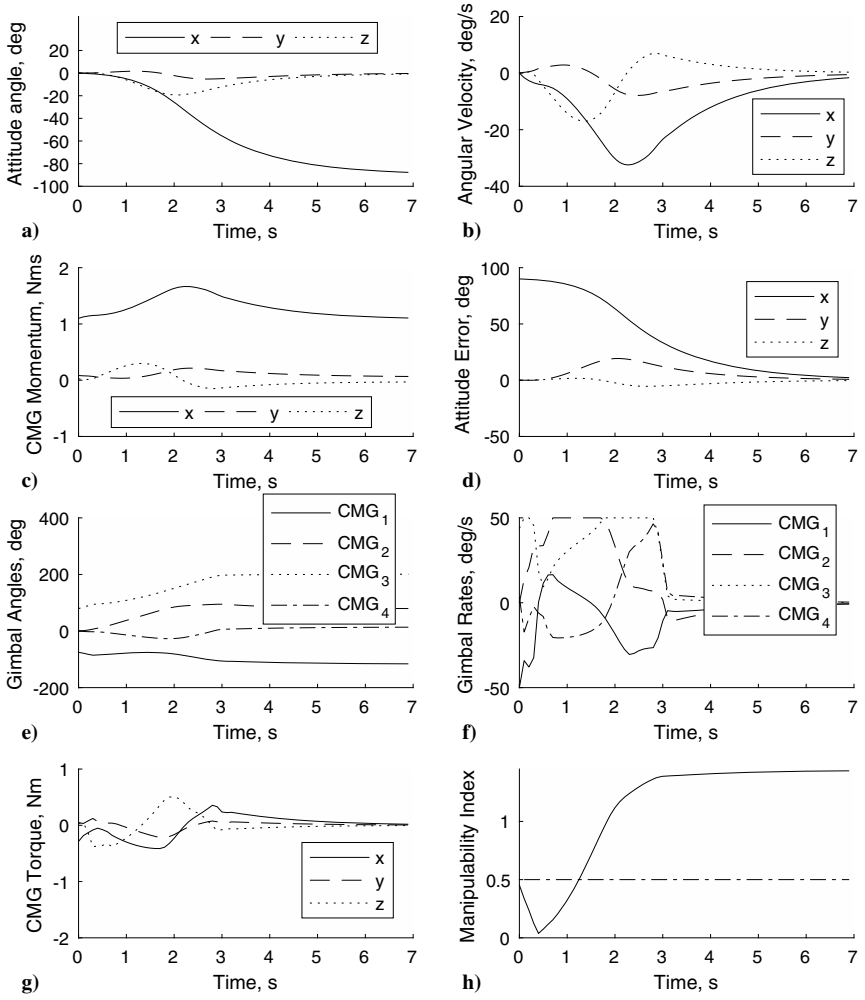

Fig. 7 Results derived using search algorithm for dynamic and kinematic (complex) models: a) attitude angle, b) angular velocity, c) CMG momentum, d) attitude error, e) gimbal angles, f) gimbal rates, g) CMG torque, and h) manipulability index.

Table 2 Complex model: percentage comparison

CF term	Change, %
w_{mean}	85.1
$T_{w<w_{\text{th}}}$	−50
$\|\boldsymbol{q}_{\text{err}}^{v}\|_{\max}$	7.5
$T_{\max\{\dot{\delta}_1,\dot{\delta}_2,\dot{\delta}_3,\dot{\delta}_4\}>\dot{\delta}_{\text{th}}}$	47.1

improve the first and the second terms. For real-life applications though, the power consumption and the motor gimbal stresses should be taken into consideration when tuning these parameters. Hence, the selection of the weights constitutes a tradeoff between the terms that are desired to be optimized. It is expected that the performances of some of output variables deteriorate. It is difficult to satisfy all terms at the same time because they are contrary, and this selection is application dependent. Moreover, the selected values of $\text{skip}_{\text{rate}}$ and skip_{th} result in a suboptimal solution for the optimization problem. Selecting lower values for $\text{skip}_{\text{rate}}$ and skip_{th} would produce a denser search with a solution closer to the optimal one.

For completeness, an additional arbitrary large angle three-axis maneuver is selected to evaluate the efficiency of the proposed method. The commanded maneuver is given by the Euler angles $[62.7, 41.6, -63.9]$ deg in 3-2-1 order. The results before and after the application of the global optimization algorithm are shown in Figs. 8 and 9, respectively; and Table 3 presents the percentage changes for the CF terms. Even though the third term related to the attitude error remains almost the same as observed in Figs. 8a and 9a, there is a 103.4% improvement in the CF value. Figure 9b shows that the gimbal rates remain saturated for a longer period of time compared to Fig. 8b in order to reorient the system to a higher-performance configuration. In Fig. 9c, the null-motion term as introduced in Eq. (22) is presented. It shows that both near the beginning and near the end of the simulation, the global optimization algorithm generates nonzero gimbal rates in the null space. This is also demonstrated by the values of the $\boldsymbol{L} = k_{\max}[0, -1, 1, 0, 0, 0, 0, 0, 1, -1]$, where the middle elements are mainly zero. As expected, the null-motion term in the case where the global optimization algorithm is not applied is zero throughout the whole simulation time (Fig. 8c); as a result, there is a 114.3% increase in the fourth term, which is proportional to the time the gimbal rates exceed the preset threshold. Significant improvements of 67 and 90.3% are presented in the mean value of the manipulability index and the time it remains below its threshold, respectively. It can be seen in Fig. 9d that the value of the index continues to increase after $t = 1.6$ s, resulting in a higher-performance configuration compared to Fig. 8d, where it dips and remains below the threshold from $t = 4.1$ s to $t = 7$ s.

B. Kinematics

In the third simulation, no dynamics are used in the calculations for the maneuver. The results obtained when the search algorithm is not applied are shown in Fig. 10. The $\boldsymbol{L}$ set is the same as in the first simulation. Figure 10a shows that the steering law drives and "locks" the system in the singular state after $t = 1.8$ s. The configuration of the gimbal angles is $[-90, 0, 90, 0]^T$, and no gimbal rates are generated by the steering law to drive the system away from this state (Fig. 10b). In addition, a nonzero momentum error in the x direction

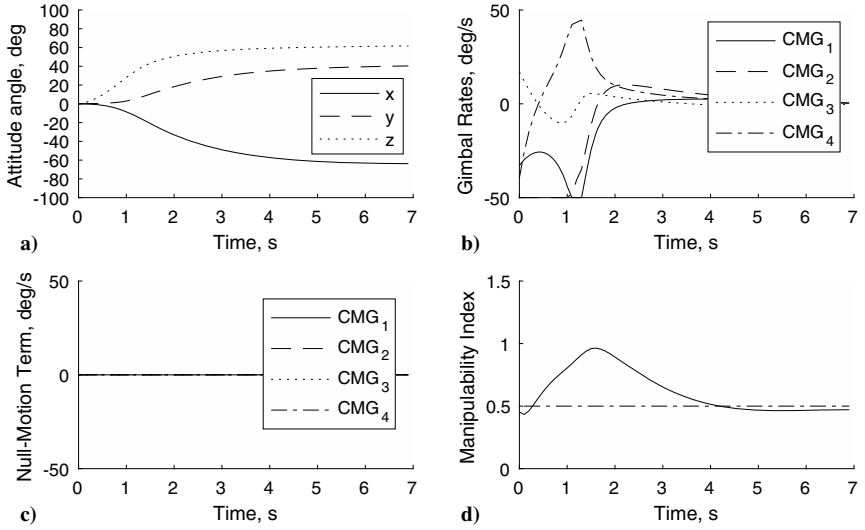

Fig. 8 Results derived without using the search algorithm for a large angle three-axis maneuver: a) attitude angle, b) gimbal rates, c) null-motion term, and d) manipulability index.

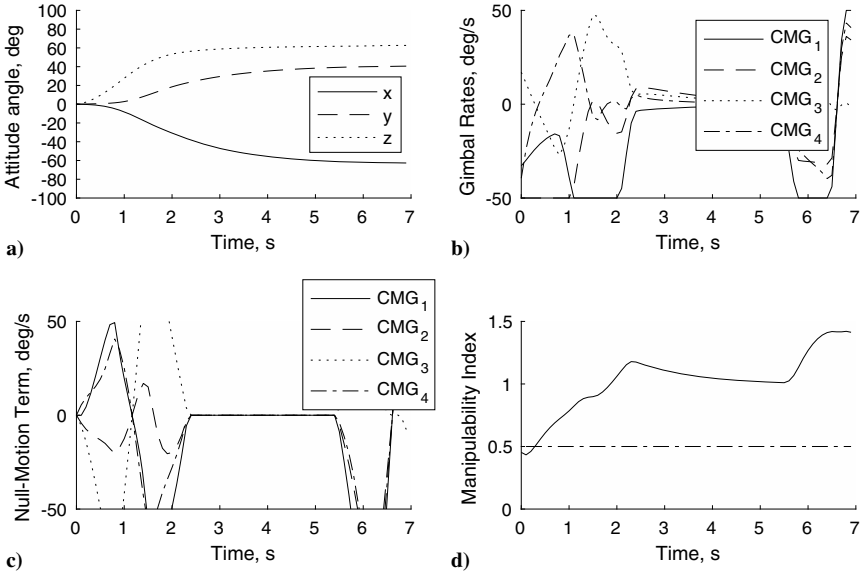

Fig. 9 Results derived using the search algorithm for a large angle three-axis maneuver: a) attitude angle, b) gimbal rates, c) null-motion term, and d) manipulability index.

Table 3 Three-axis maneuver: percentage comparison

CF term	Change, %
w_{mean}	67
$T_{w<w_{\text{th}}}$	−90.3
$\|\boldsymbol{q}_{\text{err}}^{v}\|_{\max}$	≈0%
$T_{\max\{\dot{\delta}_1,\dot{\delta}_2,\dot{\delta}_3,\dot{\delta}_4\}>\dot{\delta}_{\text{th}}}$	114.3

is presented, as shown in Fig. 10c, which is equal to 0.35 N · m · s as the total CMG momentum becomes 1.15 N · m · s along the x axis. The manipulability index drops below the threshold at $t = 1.2$ s, approaching zero at $t = 1.8$ s (Fig. 10d). The system remains locked in the singularity until the end of the simulation, as the zero value of the index indicates.

In the fourth simulation, the global optimization algorithm is applied and $\boldsymbol{L} = k_{\max}[-1, 1, 1, 1, 1, 0, -1, 0, 0, -1]$. In Table 4, the percentage change is presented for each CF term compared to the third simulation and, as in the previous model, a significant improvement in the first two terms is presented. As shown in Figs. 11a and 11b, there are noticeable differences in the gimbal angles and rates profiles compared to Figs. 10a and 10b. The algorithm drives the gimbals to a better configuration, and there is a significant increase in the time the gimbal rates remain saturated. The momentum error converges to zero in every axis compared to the previous simulation, but the SRI steering law generates error about the pitch and yaw axis as well (Fig. 11c). In total, there is a negligible increase in the momentum error, which is necessary to prevent the system from being locked in the singularity. A significant difference is also noticed in the manipulability index as presented in Fig. 11d. At $t = 2.1$ s, the minimum value of the manipulability index is obtained, which is high enough to consider that the system is not in singularity. The mean value as well as the time the index spends below the given threshold have both considerably improved. Moreover, after $t = 4$ s, when the momentum error has been eliminated, the optimization algorithm continues to improve the performance measure, modifying the gimbal angles. Specific measures related to the attitude error and/or the

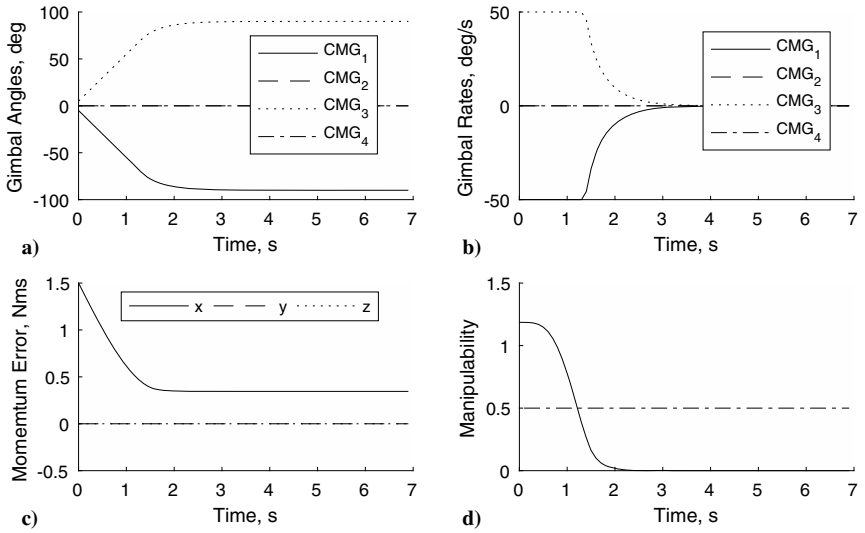

Fig. 10 Results derived without using the search algorithm for kinematic model: a) gimbal angles, b) gimbal rates, c) momentum error, and d) manipulability index.

Table 4 Kinematics-only model: percentage comparison

CF term	Change, %
w_{mean}	411
$T_{w<w_{\text{th}}}$	−60
$\|\boldsymbol{q}_{\text{err}}^{v}\|_{\max}$	0.64
$T_{\max\{\dot{\delta}_1,\dot{\delta}_2,\dot{\delta}_3,\dot{\delta}_4\}>\dot{\delta}_{\text{th}}}$	235.7

manipulability index could be taken into consideration in applications where the power demands do not allow such an aggressive gimbal rates profile. For example, a modification to stop the optimization under a given attitude/momentum error threshold or above a preset manipulability value can be applied. In such cases, the assessment of the algorithm it is recommended to be done again.

For comparison, the k set before and after the interpolation is presented in Figs. 12a and 12b, where $k_{\max} = 0.7$. Seventy values are obtained, over the 10 initial values derived by the tree depth.

A linear interpolation is used for simplicity, but any other interpolation method can be used. However, a cubic interpolation, for example, may change the result of the optimization algorithm, deriving a different cost function value.

The computational efficiency of the algorithm is vital for real-life applications. The numerical results from the simulations are discussed in the following. For the second simulation, there are 308 parent-to-child expansions, whereas this number becomes equal to 284 for the fourth simulation. In the first case, the solution is found near the end of the search, compared to the second case where the solution is found in the beginning of the optimization, skipping a number of nodes. The mean execution times for the complex and kinematics-only models are also presented in Fig. 13a.

The mean execution time for the complex model is 4 s, in contrast to the kinematics-pnly model where the mean value is 1.7 s. This difference is expected, not only because in the fourth simulation the solution is found near the beginning of the search but mainly due to the decreased numerical complexity of the kinematics-only model. To better illustrate the computation difference, the following index is calculated:

$$I_{\text{exec}} = \frac{\text{execution time in seconds}}{\text{parent to child expansions}} \tag{28}$$

For the complex model, the index I_{exec} has 2.2 times the value of the index for the kinematics-only model, verifying that the complex model runs slower for the same parent-to-child expansions.

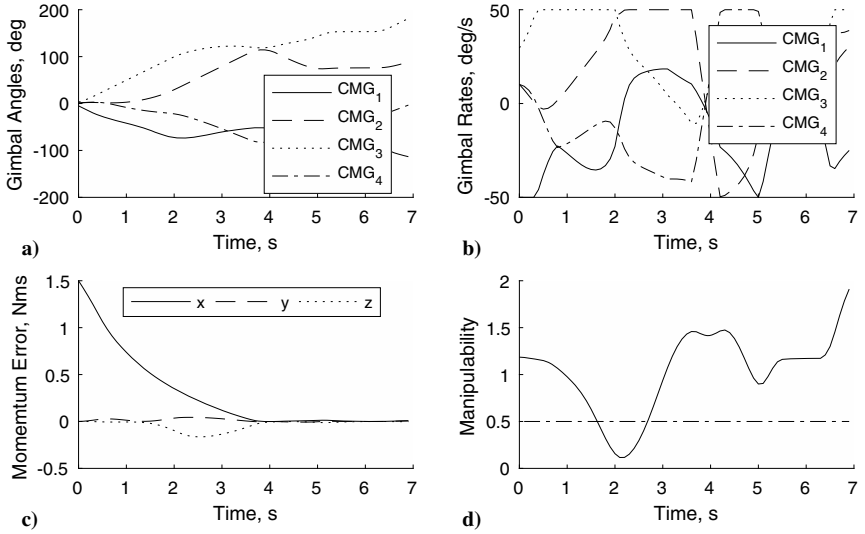

Fig. 11 Results derived using the search algorithm for kinematic model: a) gimbal angles, b) gimbal rates, c) momentum error, and d) manipulability index.

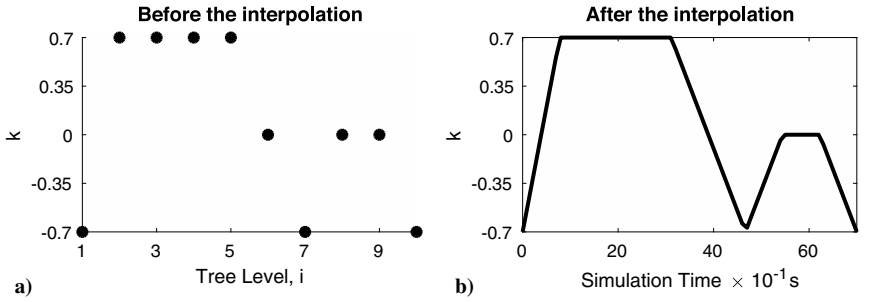

Fig. 12 *L* set a) before and b) after the interpolation.

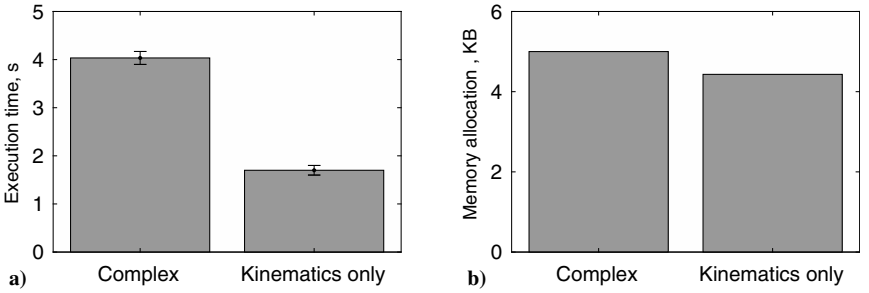

Fig. 13 Comparison among two models: a) execution time and b) memory allocation.

In Fig. 13b are given, in numbers, the memory demands for each of these two simulations. It is observed that running the simulation for the complex model allocates more memory compared to this for the simple model. In applications with memory limitations, the kinematics-only model can be exploited to predict the trajectory of the satellite. In combination with an inspection system, it is feasible to monitor if the real system follows the prediction. In the case of deviations being present (e.g., created by external disturbances), the kinematics model algorithm is executed again using, as the initial configuration, the current configuration. This way, the kinematics-only model can be used to handle a real system without dealing with the complex model and its shortcomings. However, in cases where higher memory allocation and execution time are allowed, the complex model is preferable because the in-between monitoring checks can be skipped.

In comparison with the approach used in Refs. [25,26], our method clearly has an advantage over the execution time and the memory needs. There is a 60.7% improvement in the I_{exec}, and the comparison is held for the kinematics-only model in order to be comparable to the model used in the literature. The storing precision in the previous study is limited to 1 B per variable; whereas in this paper, the precision is 8 B per variable. This corresponds to approximately 950 KB compared to the 4.4 KB used in this work. This is expected since there is not a node visit histogram to adjust the number of children skipped. The proposed algorithm handles the complexity of the problem using the variable search density approach without requiring a large amount of memory. A histogram demands a significant amount of storing variables that is proportional to the total number of nodes. Moreover, the execution time as well as the computational resources needed by the algorithm can be adapted, adjusting only two variables: $\text{skip}_{\text{rate}}$ and skip_{th}. For example, decreasing the skip_{th} increases the execution time and the parent-to-child expansions. On the other hand, a larger skip_{th} value will better suit applications where the execution speed is vital. In this case, the result will be clearly suboptimal.

The CF has been selected as a fraction whose numerator is desirable to be maximized and the denominator to be minimized. The only case for the denominator to be nearly zero is when all its terms are close to zero. This implies that the commanded maneuver is near the current attitude, the SRI does not create any deviation from the desired maneuver, the gimbal rates are below the saturation limit, and the manipulability index is above the preset threshold through the whole simulation time. In this paper, the optimization algorithm is used to determine the null space motion for larger maneuvers that pass near singular states where it is rare for all these terms to be zero at the same time. If this happens, an exception handling mechanism is required to keep track of these states and prevent calculation errors. In such cases, it should be taken into consideration that it is possible to avoid a singular state due to the small computational residuals derived by the simulation environment, and not by the actual control law, resulting in wrong conclusions. In this paper, the point where the algorithm begins to consider a state singular is described by the manipulability threshold w_{th}, the value of which is selected to be 0.5, which is far enough from the ideal theoretical value of zero. Moreover, the singularity escape in Fig. 6 when the manipulability index goes to zero is not related to numerical errors, but it is a consequence of the large angle errors provided by the SRI application.

It is possible to use the same CF to compare the same maneuver for different null space paths. However, altering the maneuver, the results are not comparable, mainly due to the third term of the CF that includes the controller error; in such cases, the third term can be ignored. Additionally, the CF could be simplified to optimizing the minimum value of the manipulability index across the trajectory as long as there is a singularity-free path for the desired maneuver. Otherwise, the maximum attitude deviation should be taken into consideration, especially for real-life applications. The exploratory character of the current study does not demand the enforcement of such limitations in the attitude error. Near singularities, the actual gimbal trajectory is possible to deviate significantly from the propagated profile upon which the optimum null-motion profile was based. Thus, a code modification to adjust the size of the $\boldsymbol{L}$ set according to the manipulability index, and thus the approach to singularity, would significantly improve the reliability of the method. Furthermore, allowing more than three distinct values for the null space motion combined with a polynomial interpolation would result in a smoother decision profile, which is more appropriate for real applications.

VI. Conclusions

In this paper, a global search optimization method is proposed. It makes use of the manipulability index, the time spent in the vicinity of singularity, the quaternion error, and the gimbal rates to adjust the null motion upon the singularity robust inverse steering law. A ternary tree structure is used for the implementation, and the results indicate

that the proposed method is capable of reconfiguring efficiently the four-control-moment-gyroscope cluster with respect to a cost function that exploits information across the trajectory of an arbitrary desired maneuver in order to avoid an elliptic singular state. Such a singularity cannot be avoided through null motion after the system is locked in this state, highlighting the importance of the global steering approach. Significant improvement is observed both in the kinematics-only and the complex models regarding the manipulability related terms compared to the case where no null motion is added. The quaternion error presents a slight increase, whereas the gimbal rates remain saturated for a longer period of time because the null motion is exploited. This effect can be reduced, either changing the value of $k_{\max}$ or the corresponding cost function coefficient.

This work can be used either offline (for inspection of the motion before applying the commands to the satellite) or online (demonstrating an easily adapted application to the situation needs). It does not use a node visit histogram, as used in previous applications to adjust the number of the children skipped, resulting in lower computational cost. It provides a novel solution to optimizing long trajectories because the desired maneuver can easily be divided in an arbitrary number of steps, whereas the computational resources required by the algorithm can easily be adjusted by tuning only two variables. To further this work, a more tight coding of the search algorithm could considerably speed up the execution time, enabling real-time operations with results closer to the optimal solution. Moreover, a modification to allow a variable $\boldsymbol{L}$ set length with more than three distinct values is also reserved for future investigation.

References

[1] Roser, X., and Sghedoni, M., "Control Moment Gyroscopes (CMG's) and their Application in Future Scientific Missions," *Spacecraft Guidance, Navigation and Control Systems, European Space Agency (ESA) Special Publication*, edited by B. Kaldeich-Schuermann, Vol. 381, ESTEC, Noordwijk, the Netherlands, 1997, p. 523, http://adsabs.harvard.edu/full/1997ESASP.381.523R [retrieved 4 Sept. 2020].

[2] Defendini, A., Lagadec, K., Guay, P., Blais, T., and Griseri, G., "Low Cost CMG-Based AOCS Designs," *Spacecraft Guidance, Navigation and Control Systems*, edited by B. Schürmann, Vol. 425, European Space Agency (ESA) Special Publication, ESTEC, Noordwijk, the Netherlands, 2000, p. 393, http://adsabs.harvard.edu/full/2000ESASP.425.393D [retrieved 4 Sept. 2020].

[3] Wie, B., *Space Vehicle Dynamics and Control*, AIAA, Reston, VA, 2008. https://doi.org/10.2514/4.860119

[4] Lappas, V., Steyn, W. H., and Underwood, C., "Design and Testing of a Control Moment Gyroscope Cluster for Small Satellites," *Journal of Spacecraft and Rockets*, Vol. 42, No. 4, 2005, pp. 729–739. https://doi.org/10.2514/1.7308

[5] Mumm, E., Davis, K., Mahin, M., Neal, D., and Hayes, R., "Miniature Control Moment Gyroscope Development," *2014 Institute of Electrical and Electronics Engineers (IEEE) Aerospace Conference*, IEEE, Piscataway, NJ, 2014, pp. 1–9. https://doi.org/10.1109/AERO.2014.6836474

[6] Margulies, G. A. J. N., "Geometric Theory of Single-Gimbal Control Moment Gyro Systems," *Journal of the Astronautical Sciences*, Vol. 26, No. 2, 1978, pp. 159–191.

[7] Wie, B., "Singularity Escape/Avoidance Steering Logic for Control Moment Gyro Systems," *Journal of Guidance, Control, and Dynamics*, Vol. 28, No. 5, 2005, pp. 948–956. https://doi.org/10.2514/1.10136

[8] Wie, B., Bailey, D., and Heiberg, C., "Singularity Robust Steering Logic for Redundant Single-Gimbal Control Moment Gyros," *Journal of Guidance, Control, and Dynamics*, Vol. 24, No. 5, 2001, pp. 865–872. https://doi.org/10.2514/2.4799

[9] Yoshikawa, T., "Manipulability of Robotic Mechanisms," *International Journal of Robotics Research*, Vol. 4, No. 2, 1985, pp. 3–9. https://doi.org/10.1177/027836498500400201

[10] Patel, S., and Sobh, T., "Manipulator Performance Measures—A Comprehensive Literature Survey," *Journal of Intelligent and Robotic Systems*, Vol. 77, No. 3, 2015, pp. 547–570. https://doi.org/10.1007/s10846-014-0024-y

[11] Richie, D. J., Lappas, V. J., and Palmer, P. L., "Sizing/Optimization of a Small Satellite Energy Storage and Attitude Control System," *Journal of Spacecraft and Rockets*, Vol. 44, No. 4, 2007, pp. 940–952. https://doi.org/10.2514/1.25134

[12] Richie, D. J., Lappas, V. J., and Prassinos, G., "A Practical Small Satellite Variable-Speed Control Moment Gyroscope for Combined Energy Storage and Attitude Control," *Acta Astronautica*, Vol. 65, No. 11, 2009, pp. 1745–1764. https://doi.org/10.1016/j.actaastro.2009.05.005

[13] Yoon, H., and Tsiotras, P., "Spacecraft Adaptive Attitude and Power Tracking with Variable Speed Control Moment Gyroscopes," *Journal of Guidance, Control, and Dynamics*, Vol. 25, No. 6, 2002, pp. 1081–1090. https://doi.org/10.2514/2.4987

[14] Yoshihara, H., and Takahashi, M., "Optimal Power Management Considering Attitude Control and Battery Deterioration Control for Spacecraft with VSCMG/IPACS," *AIAA SciTech 2020 Forum*, AIAA Paper 2020-1200, 2020, pp. 1–13. https://doi.org/10.2514/6.2020-1200

[15] Sasaki, T., Alcorn, J., Schaub, H., and Shimomura, T., "Convex Optimization for Power Tracking of Double-Gimbal Variable-Speed Control Moment Gyroscopes," *Journal of Spacecraft and Rockets*, Vol. 55, No. 3, 2018, pp. 541–551. https://doi.org/10.2514/1.A33944

[16] Sasaki, T., Shimomura, T., and Schaub, H., "Robust Attitude Control Using a Double-Gimbal Variable-Speed Control Moment Gyroscope," *Journal of Spacecraft and Rockets*, Vol. 55, No. 5, 2018, pp. 1235–1247. https://doi.org/10.2514/1.A34120

[17] Stevenson, D., and Schaub, H., "Nonlinear Control Analysis of a Double-Gimbal Variable-Speed Control Moment Gyroscope," *Journal of Guidance, Control, and Dynamics*, Vol. 35, No. 3, 2012, pp. 787–793. https://doi.org/10.2514/1.56104

[18] Vadali, S. R., Walker, S. R., and OH, H.-S., "Preferred Gimbal Angles for Single Gimbal Control Moment Gyros," *Journal of Guidance, Control, and Dynamics*, Vol. 13, No. 6, 1990, pp. 1090–1095. https://doi.org/10.2514/3.20583

[19] Geshnizjani, R., Kornienko, A., Ziegler, T., Loehr, J., and Fichter, W., "Optimal Initial Gimbal Angles for Agile Slew Maneuvers with Control Moment Gyroscopes," *AIAA SciTech 2019 Forum*, AIAA Paper 2019-0936, 2019, pp. 1–10. https://doi.org/10.2514/6.2019-0936

[20] Nanamori, Y., and Takahashi, M., "Steering Law of Control Moment Gyros Using Optimization of Initial Gimbal Angles for Satellite Attitude Control," *Nihon Kikai Gakkai Ronbunshu, C Hen/Transactions of the Japan Society of Mechanical Engineers, Part C*, Vol. 74, No. 11, 2008, pp. 2698–2704. https://doi.org/10.1299/kikaic.74.2698

[21] Qian, Z., and Guojin, T., "Technical Note: Space Station Zero Propellant Maneuver Path Planning Considering SGCMG Saturation and Singularity," *Journal of the Astronautical Sciences*, Vol. 61, No. 3, 2014, pp. 305–318. https://doi.org/10.1007/s40295-014-0023-z

[22] Cui, P., He, J., Cui, J., and Li, H., "Improved Path Planning and Attitude Control Method for Agile Maneuver Satellite with Double-Gimbal Control Moment Gyros," *Mathematical Problems in Engineering*, Vol. 2015, Jan. 2015, pp. 1–11. https://doi.org/10.1155/2015/878724

[23] Geng, Y., Hou, Z., and Huang, S., "Global Singularity Avoidance Steering Law for Single-Gimbal Control Moment Gyroscopes," *Journal of Guidance, Control, and Dynamics*, Vol. 40, No. 11, 2017, pp. 3027–3036. https://doi.org/10.2514/1.G002331

[24] Jia, Y., and Misra, A. K., "Trajectory Planning for a Space Robot Actuated by Control Moment Gyroscopes," *Journal of Guidance, Control, and Dynamics*, Vol. 41, No. 8, 2018, pp. 1838–1842. https://doi.org/10.2514/1.G002988

[25] Paradiso, J., *A Search-Based Approach to Steering Single Gimballed CMGs, Charles Stark* Draper Lab., Cambridge, MA, 1991.

[26] Paradiso, J. A., "Global Steering of Single Gimballed Control Moment Gyroscopes Using a Directed Search," *Journal of Guidance, Control, and Dynamics*, Vol. 15, No. 5, 1992, pp. 1236–1244. https://doi.org/10.2514/3.20974

[27] Lappas, V. J., "A Control Moment Gyro (CMG) Based Attitude Control System (ACS) for Agile Small Satellites," Ph.D. Dissertation, School of Electronics and Physical Sciences, Univ. of Surrey, Guildford, England, U.K., 2002, http://epubs.surrey.ac.uk/id/eprint/896 [retrieved 2020].

[28] Leve, F. A., Hamilton, B. J., and Peck, M. A., *Spacecraft Momentum Control Systems*, Springer International, Cham, Switzerland, 2015, pp. 143–145. https://doi.org/10.1007/978-3-319-22563-0.

[29] Omagari, K., Usuda, T., and Matsunaga, S., "Design and Functional Model of CMG System for Agile Attitude Maneuver of 20 kg-Class Microsatellite," *Proceedings of 15th Workshop on Japan Aerospace Exploration Agency (JAXA) Astrodynamics and Flight Mechanics*, Inst.

of Space and Astronautical Science, Japan Aerospace Exploration Agency (JAXA/ISAS), Kanagawa Prefecture, Japan, 2006, pp. 204–209, http://www.hayabusa.isas.jaxa.jp/kawalab/astro/pdf/2005B_9.pdf [retrieved 4 Sept. 2020].

[30] Israel, A., *Generalized Inverses: Theory and Applications*, Springer, New York, 2003. https://doi.org/10.1007/b97366

[31] Nakamura, Y., *Advanced Robotics: Redundancy and Optimization*, 1st ed., Addison-Wesley Longman, Reading, MA, 1990. https://doi.org/10.5555/533662

[32] Junkins, J. L., and Schaub, H., *Analytical Mechanics of Space Systems*, 2nd ed., AIAA, Reston, VA, Jan. 2009. https://doi.org/10.2514/4.867231

[33] Wie, B., Weiss, H., and Arapostathis, A., "Quaternion Feedback Regulator for Spacecraft Eigenaxis Rotations," *Journal of Guidance, Control, and Dynamics*, Vol. 12, No. 3, 1989, pp. 375–380. https://doi.org/10.2514/3.20418

[34] Xue-Qin, C., Yun-Hai, G., Yu-Hai, M., Feng, W., and Xi-Bin, C., "Integrated Attitude Control Algorithm and Steering Law for Agile Small Satellites," *2011 6th Institute of Electrical and Electronics Engineers IEEE Conference on Industrial Electronics and Applications*, IEEE, New York, 2011, pp. 139–142. https://doi.org/10.1109/iciea.2011.5975566.

[35] Kalman, R., and Bertram, J., "Control System Analysis and Design via the Second Method of Lyapunov: (I) Continuous-Time Systems (II) Discrete Time Systems," *IEEE Transactions on Automatic Control*, Vol. 4, No. 3, 1959, p. 112. https://doi.org/10.1109/TAC.1959.1104895

[36] Nakamura, Y., and Hanafusa, H., "Inverse Kinematic Solutions with Singularity Robustness for Robot Manipulator Control," *Journal of Dynamic Systems, Measurement, and Control*, Vol. 108, No. 3, 1986, pp. 163–171. https://doi.org/10.1115/1.3143764

[37] Wie, B., "Singularity Analysis and Visualization for Single-Gimbal Control Moment Gyro Systems," *Journal of Guidance, Control, and Dynamics*, Vol. 27, No. 2, 2004, pp. 271–282. https://doi.org/10.2514/1.9167

[38] Bedrossian, N. S., Paradise, J., Bergmann, E. V., and Rowell, D., "Steering Law Design for Redundant Single-Gimbal Control Moment Gyroscopes," *Journal of Guidance, Control, and Dynamics*, Vol. 13, No. 6, 1990, pp. 1083–1089. https://doi.org/10.2514/3.20582

M. A. Ayoubi
Associate Editor